Comparison of Linear Response Theory, Projected Initial Maximum Overlap Method, and Molecular Dynamics Based Vibronic Spectra: The Case of Methylene Blue

Ali Abou Taka,[†] Shao-Yu Lu,[†] Duncan Gowland,[‡] Tim J. Zuehlsdorff,[¶] Hector H. Corzo,[†] Aurora Pribram-Jones,[†] Liang Shi,[†] Hrant P. Hratchian,[*,†] and Christine M. Isborn[*,†]

[†]*Department of Chemistry and Biochemistry, University of California Merced, Merced, CA 95343, USA*

[‡]*Department of Physics, King's College London, London WC2R 2LS, United Kingdom*

[¶]*Department of Chemistry, Oregon State University, Corvallis, Oregon 97331, USA*

E-mail: hhratchian@ucmerced.edu; cisborn@ucmerced.edu

Abstract

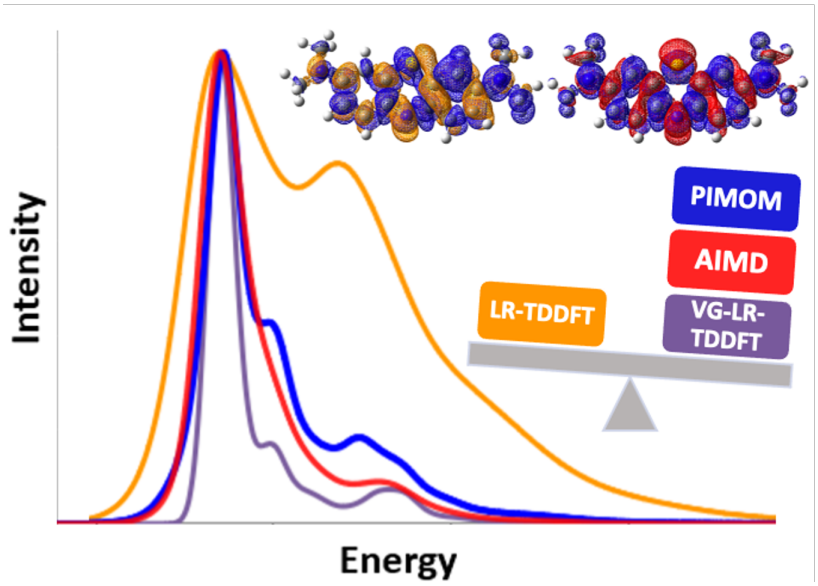

Simulation of optical spectra is essential to molecular characterization and, in many cases, critical for interpreting experimental spectra. The most common method for simulating vibronic absorption spectra relies on the geometry optimization and computation of normal modes for ground and excited states. In this report, we show that utilization of such a procedure within an adiabatic linear response theory framework may lead to state mixings and a breakdown of the Born-Oppenheimer approximation, resulting in a poor description of absorption spectra. In contrast, computing excited states via a self-consistent field method in conjunction with a maximum overlap model produces states that are not subject to such mixings. We show that this latter method produces vibronic spectra much more aligned with vertical excitation procedures, such as those computed from a vertical gradient or molecular dynamics trajectory based approach. For the methylene blue chromophore, we compare vibronic absorption spectra computed with: an adiabatic Hessian approach with linear response theory optimized structures and normal modes, a vertical gradient procedure, the Hessian and normal modes of maximum overlap method optimized structures, and excitation energy time correlation functions generated from a molecular dynamics trajectory. Due to mixing between the bright S_1 and dark S_2 surfaces near the S_1 minimum, computing the adiabatic Hessian with linear response theory time-dependent density functional theory

with the B3LYP density functional predicts a large vibronic shoulder for the absorption spectrum that is not present for any of the other methods. Spectral densities are analyzed and we compare the behavior of the key normal mode that in linear response theory strongly couples to the optical excitation while showing S_1/S_2 state mixings. Overall, our study provides a note of caution in computing vibronic spectra using the excited state adiabatic Hessian of linear response theory optimized structures, and also showcases three alternatives that are not as subject to adiabatic state mixing effects.

1 Introduction

Excited states of chromophores play an important role in a wide variety of applications, including solar energy capture, photocatalysis, bioluminescence/fluorescence, and electro-optic materials.[1–6] Predicting optical spectra and accurately characterizing excited state potential energy surfaces (PESs) affords a deeper understanding of these systems but requires accurate excited state methodologies. Even if an excited state method behaves well in regions of a vertical excitation, further challenges exist in modeling the PES near regions of a conical intersection as the Born-Oppenheimer approximation becomes less valid. In particular, adiabatic excited state methods that allow mixing of excited states can produce PESs that strongly deviate from harmonic curvature in regions of state crossings. Along an adiabatic surface that might mix excited states of different character, the nature of the state may change near regions of a conical intersection.

Due to its efficiency and relatively black box implementation, linear response theory in conjunction with time-dependent density functional theory (TDDFT) is the method of choice for most excited state calculations, including those needed for modeling optical spectroscopy.[7–9] Linear response (LR) theory avoids computation of a wave function by computing excitation energies and transition densities through the linear response formalism, defining all properties by the response of the energy or action functional.[10] Although many studies have demonstrated the ability of LR-TDDFT to accurately describe valence excited

states with a single excitation character (see Ref. 11 and references therein), the adiabatic excited states of a system built from solving the TDDFT matrix equations derived from first-order time-dependent perturbation theory and linear response theory fail to accurately describe excited states with double excitation character, so may inadequately describe the PES for such states.[12–15]

The Δ self-consistent field (ΔSCF) family of methods presents an alternative to linear response methods for computing excited states.[16–22] In contrast to linear response methods that mix excited states together to produce adiabatic surfaces, ΔSCF approaches solve for a single excited state that generally exhibits consistent character across the PES. In this way, ΔSCF excited state solutions can be considered diabatic states.

In recent years, Gill and coworkers rejuvenated the idea of converging SCF calculations as representations for excited electronic states using maximum overlap concepts.[16,17] Maximum overlap methodologies (MOM) use standard ground-state SCF algorithms modified to maximize the overlap between the occupied molecular orbitals of a user-defined SCF target and that computed in the current SCF iteration. In many instances, this procedure suffices to find stationary points in the SCF space that correspond to excited state solutions, which are often characterized as saddle points in SCF space.[23] Additionally, for non-adiabatic methods requiring a diabatic treatment of the excited state PES, similar approaches based on constrained DFT present a viable path forward for computing excited state couplings and properties.[24]

The projected initial maximum overlap method (PIMOM) has recently been shown to be a robust member of the family of MOM algorithms. In this MOM variation, the algorithm drives the convergence of excited SCF solutions by introducing a projection operator that preserves molecular orbital occupations corresponding to the target state of interest.[25,26]

The use of the ΔSCF approach comes with advantages and disadvantages that depend on the system's excited state of interest. One of the main advantages of ΔSCF approaches is that the computational expense of the simulation is no more than a regular ground-

state Hartree-Fock or DFT calculation. Also, these approaches may produce a proper wave function; thus evaluating molecular properties of excited states is much more straightforward than in linear response theory, as all ground-state machinery can be used directly. The MOM family of methods is able to model challenging excited states, including double excitations.[23] On the other hand, ΔSCF approaches may suffer from variational collapse and have a strong dependency on the user-provided target guess. Another limitation of using ΔSCF approaches is that the calculations are state-specific, requiring a separate SCF calculation for each excited state.

Vibronic spectra can be computed with a variety of methods. Perhaps the most popular method for larger molecules is to parametrize harmonic potentials by computing the Hessian and then using the frequencies and displacements from normal modes computed at the ground- and excited-state minima, which takes the form of a generalized Brownian oscillator model. Within this harmonic approximation to the PES, the nuclear wave functions are known, and overlaps can be calculated between ground- and excited-state wave functions to determine the intensity of vibronic transitions, yielding the exact Franck-Condon spectrum for the harmonic surfaces.[27] This Hessian-based approach can easily accommodate Duschinsky effects or normal mode mixing upon electronic excitation.[28]

The substantial computational cost associated with the excited-state Hessian calculation is avoided with the vertical gradient approach, where the excited-state gradient is computed at the ground-state minimum and the normal modes and frequencies are assumed to be the same for the excited state as in the ground state.[29–31] The vertical gradient method may be particularly well-suited to computing spectra if the excited-state minimum is close to a conical intersection, as adiabatic excited state methods may yield substantial changes in PES character in this region.[32,33] In a study by Avila Ferrer and Santoro comparing vertical gradient and adiabatic Hessian approaches for the computation of vibronic spectra, the authors concluded that discrepancies in the vibronic spectra of these two methods are diagnostic for the failure of the harmonic approximation and/or a breakdown of the Born–Oppenheimer

approximation due to geometry-dependent mixing of states.[34]

An alternative approach to the direct computation of wave function overlap is the use of energy gap time correlation functions within a cumulant expansion to the linear response function.[35] These energy gap time correlation functions can be constructed from a time-series of excitation energies computed for configurations along a molecular dynamics trajectory, usually obtained from ground-state dynamics that sample the region of vertical excitation.[36,37] Molecular dynamics (MD) trajectories generally treat the nuclei classically and thus produce classical correlation functions, but the necessary quantum correlation functions can be approximated with a quantum correction factor.[38–41] Although the cumulant expansion to the linear response function is formally exact, in practice it is generally truncated at second or third order. Truncation at second order is exact for a system with a Gaussian distribution of energy gap fluctuations, which occurs for displaced harmonic potentials of the same frequency. Changing the frequency or rotating the potentials may introduce nonlinear coupling that can be partially captured by the third order term, which also is able to incorporate some effects of anharmonic potentials.[36,42] In addition to being able to sample anharmonic nuclear configurations, a dynamic MD energy gap time correlation function based approach also describes coupling to an explicit environment.[36,37,42–44]

In this work, we compare the above mentioned methods in modeling the excited states and linear absorption vibronic spectrum of the methylene blue chromophore in vacuum. A recent study by de Queiroz *et al.* of the $S_0 \rightarrow S_1$ Franck-Condon vibronic spectrum *in vacuo*, obtained at the linear response TDDFT B3LYP/def2-SV(P) level of theory, predicts a very large vibronic shoulder.[45] However, very recent work by some of the authors suggests that the LR-TD-B3LYP $S_0 \rightarrow S_1$ vibronic shoulder may be due to S_1/S_2 state mixing and a potential breakdown of the Born-Oppenheimer approximation.[46] We here investigate this state mixing possibility more thoroughly and also present the ability of PIMOM to approximate excited states and absorption spectra that are not subject to state mixing and thus find that PIMOM is more amenable than LR-TDDFT to the use of the excited state Hessian

for predicting vibronic spectra. After giving a brief overview of PIMOM and various methods for computing absorption spectra, we compare excited states computed with adiabatic LR-TDDFT and PIMOM for methylene blue. We then showcase the simulated vibronic spectra computed with the following approaches: adiabatic Hessian LR-TDDFT, vertical gradient LR-TDDFT, Hessian PIMOM, and a truncated cumulant expansion of the linear response function obtained from computed energy gaps along an MD trajectory. Computation of the spectral density reveals which normal mode couples most strongly to the optical excitation and is responsible for the large vibronic shoulder predicted by adiabatic Hessian LR-TD-B3LYP. Analysis of this normal mode shows that LR-TD-B3LYP predicts S_1/S_2 state mixing along this coordinate. In contrast, PIMOM predicts an S_1 PES of consistent character and produces a vibronic spectrum accordant with vertical gradient and molecular dynamics trajectory approaches.

2 Theoretical Background

2.1 Self-consistent field with the projected initial maximum overlap method - PIMOM

As alternatives to linear response theory, ΔSCF approaches calculate excited states with ground state computational models and cost.[17,21–23,47–52] Promoting a single or multiple electrons from the occupied to the virtual space yields an approximate representation of a singly- or multiply- excited state. Although using SCF for computing excited state properties may be highly attractive, standard SCF algorithms in most cases are not able to access excited state solutions due to variational collapse.[47,48] Overcoming this challenge has received increased attention in recent years. One family of techniques that has shown great success is that of the maximum overlap methods.[17,23,51] A recent member of this family reported by a group of us is the projected initial maximum overlap method (PIMOM).[25]

PIMOM provides an alternative aufbau principle by which the occupied molecular or-

bitals (MOs) are chosen based on the largest overlap with the provided target determinant's occupied sub-space rather than on their one-electron orbital energies. More specifically, occupied/virtual permutations are employed at each SCF cycle, based on the amplitude of each of the current molecular orbitals projected onto the target system's occupied molecular orbital sub-space. In the PIMOM scheme, a density projection operator, $\mathscr{P}^{\text{target}}$, is used to define the alternative aufbau metric,

$$\mathscr{P}^{\text{target}} = \sum_i |i^{\text{target}}\rangle \langle i^{\text{target}}| . \tag{1}$$

This projection operator in the current-MO basis at each SCF cycle is

$$P_{pq}^{\text{target}} = \langle p| \mathscr{P}^{\text{target}} |q\rangle = \sum_i \langle p|i^{\text{target}}\rangle \langle i^{\text{target}}|q\rangle, \tag{2}$$

where $|i^{\text{target}}\rangle$ is the initial set of MOs, $|p\rangle$ and $|q\rangle$ are the current set of MOs.

Equation (2) can be further decomposed to

$$P_{pq}^{\text{target}} = \sum_i \sum_{\mu\nu} \sum_{\lambda\sigma} C_{\mu p} S_{\mu\lambda} C_{\lambda i}^{\text{target}} C_{\sigma i}^{\text{target}} S_{\sigma\nu} C_{\nu q}, \tag{3}$$

where $\mathbf{C}$ and $\mathbf{C}^{\text{target}}$ are the current and target sets of MO coefficients, respectively. $\mathbf{S}$ is the atomic orbital (AO) overlap matrix.

Given that the MO basis is orthonormal, P_{pq}^{target} can be used to give the target density's gross Mulliken populations partitioned into the current MO basis. With this in mind, the PIMOM model defines a modified aufbau metric, s_p, as

$$s_p = \sum_q P_{pq}^{\text{target}}. \tag{4}$$

Thus, the MOs with the largest s_p are chosen to be occupied.

2.2 Computing optical spectra

In this subsection, we outline two main approaches for computing linear vibronic absorption spectra. The first approach computes the linear response function directly from the harmonic oscillator wave functions as determined from the normal modes that parametrize a generalized Brownian oscillator model. As the wave functions of the ground and excited state are directly computed, such an approach is exact within the harmonic Franck-Condon principle. The second approach approximates the linear response function based on a truncated cumulant expansion, in which each term in the cumulant expansion can be determined from computation of an energy gap time correlation function. The energy gap time correlation functions can be determined exactly for a generalized Brownian oscillator model and can also be computed directly from an MD trajectory.

2.2.1 Linear absorption vibronic spectra in the harmonic Franck-Condon or vertical gradient approach

The generalized Brownian oscillator model (GBOM) consists of harmonic potentials of differing frequency that may be rotated with respect to each other. In the GBOM, the nuclear Hamiltonians for the electronic ground and excited state with N_j vibrational modes can be written as:

$$H_g(\hat{\mathbf{q}}_g, \hat{\mathbf{p}}_g) = \frac{1}{2}\sum_j^{N_j} \left[\hat{p}_{g,j}^2 + \omega_{g,j}^2 \hat{q}_{g,j}^2\right], \tag{5a}$$

$$H_e(\hat{\mathbf{q}}_e, \hat{\mathbf{p}}_e) = \frac{1}{2}\sum_j^{N_j} \left[\hat{p}_{e,j}^2 + \omega_{e,j}^2 \hat{q}_{e,j}^2\right] + \Delta_{\text{eg}}^0, \tag{5b}$$

where the ground and excited state normal modes are related through the linear transformation:

$$\hat{q}_{g,i} = \sum_j^{N_j} J_{ij}\hat{q}_{e,j} + K_i. \tag{6}$$

Here, K_i is the shift vector describing the displacement between ground- and excited-state PES minima, Δ_{eg}^0 is the energy gap between the ground- and excited-state minima, and $\mathbf{J}$ is the Duschinsky rotation matrix. Both the difference in curvature, with $\omega_{g,i} \neq \omega_{e,i}$, and the Duschinsky rotation lead to non-Gaussian energy gap fluctuations.[36]

However, given ground- and excited-state optimized structures, the Hessian may be computed. Computing the harmonic normal modes and corresponding wave functions, displacements, and a Duschinsky rotation allows exact computation of the absorption vibronic spectrum for a GBOM within the Franck-Condon approach, wherein overlaps between ground- and excited-state harmonic oscillator wave functions determine the intensity of vibronic peaks in the spectrum,

$$\begin{aligned} \sigma_{\text{FC}}(\omega) \propto \omega |V_{ge}|^2 \sum_{v_g} \rho(v_g) \sum_{v_e} \left| \langle \phi_{v_g} | \phi_{v_e} \rangle \right|^2 \\ \times \mathcal{N}\left(\omega - \left[\omega_{v_e} - \omega_{v_g}\right], s\right). \end{aligned} \tag{7}$$

Here V_{ge} is the transition dipole between the ground and excited electronic states, $|\phi_{v_g}\rangle$ and $|\phi_{v_e}\rangle$ denote nuclear wave functions, and ω_{v_g} and ω_{v_e} represent the corresponding total energy of the system in the ground and excited state. The Boltzmann population $\rho(v_g)$ determines the occupation of the ground-state vibrational levels at a given temperature. The Franck-Condon overlap integral $\langle \phi_{v_g} | \phi_{v_e} \rangle$ gives the intensity of the vibronic transitions between different vibrational levels. This harmonic Franck-Condon approach can be implemented using time-dependent (effective for large multi-mode systems) and time-independent (sum over states, effective for smaller systems) techniques, with extension to Herzberg-Teller effects that include linear effects of the structure on transition dipole moment.[53–57] The broadening parameter s is chosen either in an *ad hoc* manner or can be estimated from first principles according to Marcus theory.[58]

Franck-Condon absorption spectra can also be computed within a vertical gradient approximation,[29–31] which avoids geometry optimization of the electronic excited state and instead computes the excited-state gradient at the ground-state optimized geometry, in the

Condon region, in order to approximate the location of the excited-state minimum.[29] The curvature of the excited-state potential, and therefore normal modes and frequencies, are assumed to be the same as in the ground state.

2.2.2 Linear absorption vibronic spectra in the cumulant approach: correlation functions built from a molecular dynamics trajectory or generalized Brownian oscillator model

For a two-level electronic system consisting of an electronic ground state and a single electronic excited state coupled to nuclear motion and within the Condon approximation, it is possible to write the linear absorption vibronic spectrum in terms of a cumulant expansion of the energy gap fluctuation operator $\delta U(\hat{\boldsymbol{q}}) = H_e(\hat{\mathbf{q}}_e) - H_g(\hat{\mathbf{q}}_g) - \omega_{\rm eg}^{\rm av} = U(\hat{\boldsymbol{q}}) - \omega_{\rm eg}^{\rm av}$:[35]

$$\begin{aligned}\sigma(\omega) &\propto \omega |V_{ge}|^2 \mathrm{Re} \int_0^\infty \mathrm{d}t\, e^{\mathrm{i}\left(\omega - \omega_{\rm eg}^{\rm av}\right)t} \\ &\times \left\langle \exp_+ \left[-\mathrm{i} \int_0^t \mathrm{d}\tau\, \delta U\left[\hat{\boldsymbol{q}}(\tau)\right] \right] \right\rangle \\ &\propto \omega |V_{ge}|^2 \mathrm{Re} \int_0^\infty \mathrm{d}t\, e^{\mathrm{i}\left(\omega - \omega_{\rm eg}^{\rm av}\right)t} \exp\left[\sum_{n=2}^{\infty} g_n(t) \right].\end{aligned} \tag{8}$$

Here, $\omega_{\rm eg}^{\rm av} = \langle U(\hat{\boldsymbol{q}}) \rangle$ is the thermal average of the energy gap operator, $g_n(t)$ is the n^{th} order cumulant, and Hartree atomic units are used throughout. Here we re-express the response function as an infinite expansion with respect to cumulants (combinations of moments) of the energy gap fluctuation. We rewrite the time-ordered exponentiated integral (denoted by $\exp_+$) of the energy gap operator as the exponentiated sum of cumulants and then match terms order by order in δU. If the energy gap fluctuations are Gaussian, as is true for the quadratic potential of a simple displaced harmonic oscillator system where ground and excited state energy surfaces have the same curvature, the cumulant expansion in Eq. (8) can be exactly truncated at second order.[35] For more realistic PESs, or if the frequencies of the two potentials are different or rotated with respect to each other, higher order cumulants will contribute to the lineshape.[36,59] The cumulants can be expressed in terms of time-ordered

integrals of increasing orders of quantum time-correlation functions $C_{\delta U}$ of the energy gap fluctuation operator δU. For the second order cumulant, we can write

$$g_2\left[C_{\delta U}^{\{2\}}\right](t) \;=\; \int_0^t \mathrm{d}\tau_2 \int_0^{\tau_2} \mathrm{d}\tau_1\, C_{\delta U}^{\{2\}}(\tau_2-\tau_1), \tag{9}$$

where

$$C_{\delta U}^{\{2\}}(t) \;=\; \langle \delta U(t)\delta U(0)\rangle\,, \tag{10}$$

with analogous expressions for higher order quantum correlation functions.[59]

The second order cumulant contribution $g_2(t)$ can be written in terms of the spectral density $\mathcal{J}(\omega)$ by switching into Fourier space:[35]

$$\begin{aligned} g_2(t) \;=\; & \frac{1}{\pi}\int_0^\infty \mathrm{d}\omega\; \frac{\mathcal{J}(\omega)}{\omega^2}\left[\coth\left(\frac{\beta\omega}{2}\right)[1-\cos(\omega t)]\right. \\ & \left. -\mathrm{i}[\sin(\omega t)-\omega t]\right], \end{aligned} \tag{11}$$

with $\beta = 1/(k_{\mathrm{B}}T)$ and

$$\mathcal{J}(\omega) = \mathrm{i}\theta(\omega)\int \mathrm{d}t\; e^{\mathrm{i}\omega t}\;\mathrm{Im}\; C_{\delta U}(t). \tag{12}$$

A similar expression can be derived[36] for the third order correction $g_3(t)$. As we have recently demonstrated,[36] the third order cumulant correction can provide significant improvements in the absorption lineshapes of systems with moderately anharmonic potentials. The exact quantum correlation function $C_{\delta U}(t)$ is in general impossible to compute except for simple model systems. In previous work, some of the authors have derived and implemented the exact quantum time correlation functions needed for the second order and the third order cumulant terms for the GBOM, including Duschinsky rotation effects.[36] For a more realistic system, $C_{\delta U}(t)$ can be computed from an MD trajectory, where it is approximately reconstructed from its classical counterpart, $C^{\mathrm{cl}}(t)$ using quantum correction factors.[38–40] In this

work, we use the harmonic quantum correction factor,[39,41] yielding

$$\mathcal{J}(\omega) \approx \theta(\omega)\frac{\beta\omega}{2}\int \mathrm{d}t\; e^{\mathrm{i}\omega t}\; C^{\mathrm{cl}}(t), \tag{13}$$

where $\beta = 1/k_{\mathrm{B}}T$ and $\theta(\omega)$ is the Heaviside step function.

3 Computational details

3.1 Geometry optimization, normal mode computation, and Franck-Condon vibronic spectral calculations

All ground- and excited-state structures were optimized using the hybrid B3LYP and the range-separated hybrid CAM-B3LYP functionals with the 6-31+G* Pople basis set,[60] with ground-state Kohn-Sham determinants tested for stability.[61,62] Excited-state calculations were carried out using the same model chemistry either within the LR formalism[8,63,64] or with the PIMOM ΔSCF method. Initial guesses, which serve as target determinants, for PIMOM ΔSCF calculations were generated by permutating ground-state molecular orbitals to resemble the desired excited-state. HOMO-LUMO MOs were permuted to generate the S_1 initial guess while HOMO-1–LUMO MOs were permuted for calculations of the S_2 state. All ΔSCF results were obtained using an implementation of the PIMOM algorithm in a local development version of Gaussian.[65] Analyses for converged electronic excited states were facilitated by using a modified form of the natural ionization orbital (NIO) model by Hratchian and coworkers.[66–68] Using the NIO model, converged electronic excited states were verified by visualizing the natural orbitals of the difference densities relative to the ground state. This scheme is analogous to the Natural Transition Orbital model of Martin,[69] but directly separates electron-hole pairs from orbital relaxation contributions in the difference density from a ΔSCF set of calculations.

We note that one inherent challenge with the ΔSCF approach to studies of one-electron

excited states is that such SCF solutions often exhibit spin symmetry breaking, which can be observed as spin-contamination. Spin contamination results when a single-determinant SCF solutions is not an eigenstate of the S^2 operator and can be described as resulting from an admixture of a desired pure spin state and *contaminating* higher spin states.[70] Preliminary calculations following protocols developed in one of our labs and considering approximate (spin) projection models to remedy impacted energies, forces, and force constants suggested that spin-contamination should not negatively impact the PIMOM based spectral simulations reported in this study.[71–78]

Molecular geometries for ground and excited states were optimized using standard methods,[79] and the reported PES minima were verified using analytical second-derivative calculations.[80,81] The methylene blue ground state S_0 optimized structure is of C_{2v} symmetry for both B3LYP and CAM-B3LYP. This C_{2v} symmetry is maintained for the S_1 minimum obtained for PIMOM/B3LYP, PIMOM/CAM-B3LYP, and LR-TDDFT/CAM-B3LYP. However, for the LR-TDDFT/B3LYP, the S_1 minimum is of C_s symmetry.

Hessian-based vibronic spectra, under the harmonic approximation, were simulated using the implementation by Bloino, Barone, and co-workers for both PIMOM and LR-TDDFT by computing the Hessian and displacements at the ground- and excited-state minima.[82] The vertical gradient Franck-Condon vibronic spectra for LR-TDDFT were also computed.[29–31] All spectra are scaled so that the λ_{max} intensities are unity.

3.2 Parametrization of generalized Brownian oscillator model

We used the ground- and excited-state geometry optimizations and normal modes from the LR-TDDFT and PIMOM calculations to construct the GBOM for methylene blue. The Franck-Condon spectrum provides the exact solution to the linear response spectrum of the GBOM. The shift vector **K** and the Duschinsky rotation matrix **J** were directly extracted from the Gaussian output file using the functionality to compute Franck-Condon spectra. The parametrized GBOM was used to construct the spectral density and the truncated

cumulant expansion–based linear absorption spectra. For the parametrized GBOM that includes Duschinsky rotation effects, we use our previously implemented analytical expressions for the exact quantum time correlation functions needed for the second order and the third order cumulant terms[36] within the MolSpeckPy package.[83]

3.3 Ab initio molecular dynamics, computation of vertical excitation energies, and energy gap correlation functions

We performed *ab initio* molecular dynamics (AIMD) simulations of methylene blue in vacuum in the NVT ensemble at $T = 300$K using target Langevin thermostats. The AIMD simulations employed a 0.5 fs time step for a 17 ps run. The AIMD calculations were carried out at the same level of theory as the ground-state geometry optimizations, employing both B3LYP and CAM-B3LYP with the 6-31+G* basis set. To compute the correlation functions needed for the linear absorption spectroscopy, we discard the first 1 ps for equilibration from AIMD trajectories and then extracted the snapshots every 2 fs from the last 16 ps of each trajectory, yielding a total of 8000 snapshots for energy gap calculations. For each snapshot, LR-TDDFT excited state calculations were performed at the corresponding level of theory.

Upon analyzing the S_1 and S_2 LR-TDDFT states along the AIMD trajectory, we find substantial excited state reordering and mixing for the LR-TD-B3LYP states. The LR-TD-CAM-B3LYP states do not mix during the trajectory. The cumulant-based approach employed here assumes a two-state model, and thus does not account for mixing between states. We therefore use the diabatization strategy outlined by Subotnik and co-workers,[84] where the transition dipole matrix $\mathbf{D}$ is defined as

$$\mathbf{D} = \begin{pmatrix} V_{01} \cdot V_{01} & V_{01} \cdot V_{02} \\ V_{01} \cdot V_{02} & V_{02} \cdot V_{02} \end{pmatrix}, \tag{14}$$

where V_{0n} is the transition dipole moment between the ground state and state n. Diagonal-

izing **D** produces two states with maximally different transition dipole moments, where the eigenvectors are then used to rotate the diagonal matrix of adiabatic excitation energies into a matrix with two diabatic excitation energies on the diagonal and their electronic coupling as the off-diagonal elements. We performed this diabatization for every snapshot along the AIMD trajectory, then used the resulting energy gaps to construct the classical autocorrelation function $C^{\mathrm{cl}}(t)$ used to determine the spectral density and AIMD based cumulant lineshapes.

Further details of the formalism and implementation of spectral densities and cumulant lineshape calculations based upon $C^{\mathrm{cl}}(t)$ can be found in recent publications by some of the authors, and are available in the MolSpeckPy package.[83]

4 Results and discussion

4.1 Comparison of PIMOM and LR-TDDFT excitation energies and difference densities

Before analyzing vibronic absorption spectra computed with different methods, it is worthwhile to examine the excitation energies computed with PIMOM and LR-TDDFT for the vertical excitation energies computed from the S_0 ground-state optimized geometry and the from the S_1 excited-state optimized geometry. At the S_0 minimum, the S_1 state is primarily HOMO $\rightarrow$ LUMO character, whereas the S_2 state is primarily HOMO-1 $\rightarrow$ LUMO. These MO occupations were used to find the corresponding PIMOM excited states and corresponding excited state optimized structures.

Table 1 shows the energy gaps between the S_1 and S_2 states computed with PIMOM and LR-TD-B3LYP for the S_0 minimum as well as for the excited-state S_1 minimum for both methods. The energy gaps between these states are larger for PIMOM than for LR-TDDFT, with LR-TD-B3LYP having a fairly small energy gap of 0.1-0.3 eV. Interestingly, for the LR-TD-B3LYP S_1 minimum, the energy gap decreases for PIMOM and increases for

Table 1: B3LYP $S_2 - S_1$ electronic energy gaps in eV at S_0, $S_1^{\text{LR-TDDFT}}$, and $S_1^{\text{LR-TDDFT}}$ optimized geometries obtained using PIMOM and LR-TDDFT approaches. Oscillator strengths (f) of S_1 and S_2 are also reported for LR-TDDFT.

Optimized Geometry	**PIMOM** $\mathbf{E_{S_2}}$-$\mathbf{E_{S_1}}$ **(eV)**	**LR-TDDFT** $\mathbf{E_{S_2}}$-$\mathbf{E_{S_1}}$**(eV)**	$\mathbf{f_{S_1}/f_{S_2}}$
$\mathbf{S_0}$	0.54	0.13	0.810/0.001
$\mathbf{S_1^{LR\text{-}TDDFT}}$	0.44	0.29	0.382/0.350
$\mathbf{S_1^{PIMOM}}$	0.52	0.10	0.796/0.003

LR-TD-B3LYP. At this LR-TD-B3LYP S_1 optimized geometry, the oscillator strength f of both the $S_0 \rightarrow S_1$ and the $S_0 \rightarrow S_2$ changes substantially, with the bright S_1 transition losing oscillator strength and the dark S_2 transition gaining oscillator strength. At this geometry, the states indicate substantial mixing due to nearly equal values of their oscillator strengths. This mixing is supported by the MO contributions, which at this geometry are a mixture of HOMO $\rightarrow$ LUMO and HOMO-1 $\rightarrow$ LUMO.

In contrast to LR-TD-B3LYP, LR-TD-CAM-B3LYP yields consistent S_1 and S_2 states for the geometries considered here, with similar S_1 to S_2 energy gaps and oscillator strengths for S_0 and both S_1 geometries, see Table 2. The LR-TD-CAM-B3LYP energy gap between S_1 and S_2 is also larger than that with LR-TD-B3LYP, suggesting less state mixing. However, PIMOM shows the opposite trend, with the S_1 to S_2 CAM-B3LYP gap being smaller than the B3LYP gap. For both functionals, the PIMOM S_1 to S_2 energy gap decreases by 0.02 eV going from the S_0 minimum to the PIMOM S_1 minimum, suggesting that PIMOM is more functional-agnostic than LR-TDDFT, as it is not subject to the inconsistent treatment of excited states of different character or adiabatic state mixing effects.

Table 2: CAM-B3LYP $S_2 - S_1$ electronic energy gaps in eV at S_0, $S_1^{\text{LR-TDDFT}}$, and $S_1^{\text{LR-TDDFT}}$ optimized geometries obtained using PIMOM and LR-TDDFT approaches. Oscillator strengths of S_1 and S_2 are also reported for LR-TDDFT.

Optimized Geometry	**PIMOM** $\mathbf{E_{S_2}}$-$\mathbf{E_{S_1}}$ **(eV)**	**LR-TDDFT** $\mathbf{E_{S_2}}$-$\mathbf{E_{S_1}}$**(eV)**	$\mathbf{f_{S_1}/f_{S_2}}$
$\mathbf{S_0}$	0.49	0.38	0.959/0.006
$\mathbf{S_1^{LR\text{-}TDDFT}}$	0.47	0.36	0.930/0.006
$\mathbf{S_1^{PIMOM}}$	0.47	0.34	0.931/0.006

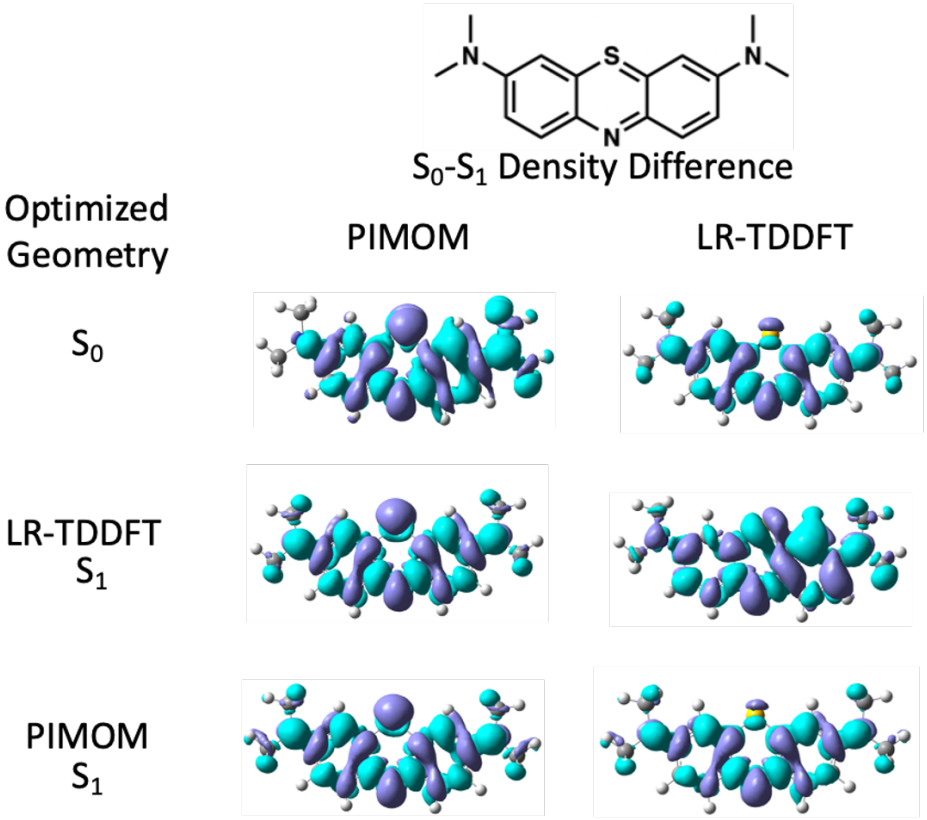

Figure 1: The structure of the methylene blue chromophore and the B3LYP density difference between the ground and S_1 excited state at the ground state S_0, LR-TDDFT S_1, and PIMOM S_1 optimized geometries.

To further illustrate the behavioral difference between LR-TDDFT and PIMOM, the B3LYP electron density difference between the ground and S_1 excited state densities computed at the LR-TDDFT S_1, PIMOM S_1, and ground state optimized geometries are shown in Fig. 1. PIMOM produces a consistent density difference for all three optimized geometries, indicating that the treatment of the S_1 state is consistent for all three geometries. The LR-TD-B3LYP density differences obtained at the ground state and the PIMOM optimized geometries are similar to the density differences predicted by PIMOM. In contrast, the LR-TD-B3LYP difference densities shows qualitatively different character for the LR-TD-B3LYP S_1 minimum, with notable symmetry breaking, demonstrating that PIMOM and LR-TDDFT produce S_1 states of substantially different character for this geometry. The CAM-B3LYP density differences (shown in the SI, Fig. S1) are in excellent agreement for both PIMOM and LR-TDDFT for all geometries. The CAM-B3LYP PIMOM density differences are very similar to the B3LYP PIMOM density differences, again showing that the PIMOM method is not as subject to the functional dependencies of the LR-TDDFT procedure.

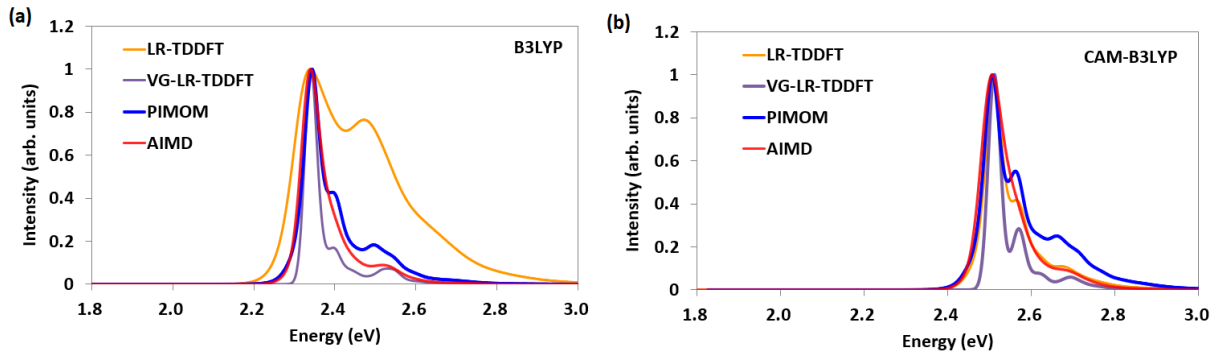

Figure 2: (a) B3LYP and (b) CAM-B3LYP $S_0 \rightarrow S_1$ vibronic spectra computed with: the adiabatic Hessian from linear response TDDFT (LR-TDDFT), the vertical gradient from LR-TDDFT (VG-LR-TDDFT), the Hessian from PIMOM, and LR-TDDFT energy gap time correlation function from the ground-state AIMD trajectory (AIMD). Note that spectra are energetically aligned as mentioned in the main text.

4.2 Linear absorption spectra

The four spectral methods, which include adiabatic Hessian LR-TDDFT, vertical gradient LR-TDDFT, Hessian based PIMOM, and AIMD, are compared in Fig. 2 for B3LYP and CAM-B3LYP. The vibronic spectra for (PIMOM, AIMD) are shifted by (0.83 eV, -0.05 eV) for B3LYP and (0.76 eV, -0.03 eV) for CAM-B3LYP, respectively. These shifts make the energy of the 0-0 transition uniform, allowing better comparison of lineshape.

Each of the methods examined here employs different approximations. LR-TDDFT is an adiabatic, perturbative approach that does not properly describe states of double excitation character. Additionally, adiabatic Hessian and normal mode calculation at the LR-TDDFT excited state minimum may not be well-behaved if PESs mix together in this region. In such cases, a harmonic approximation may be insufficient to properly describe the adiabatic PES. In contrast, the vertical gradient approach avoids the computation of the excited-state minimum and normal modes, instead computing only the excited-state gradient at the optimized geometry of the ground state. Although this vertical gradient approach is often assumed to be less accurate than the full normal mode calculation at the S_1 excited state minimum, the vertical gradient approach may be better suited for modeling absorption spectra than the adiabatic Hessian approach if the S_1 minimum is near a surface crossing. Indeed, in Fig. 2a, we see significant differences in the spectra computed with the adiabatic Hessian LR-TD-B3LYP approach obtained with full geometry optimization and normal mode computation at the LR S_1 minimum, compared to that obtained with the vertical gradient approach. Note that both of these LR methods use the same ground-state normal modes. Thus, the only difference is the treatment of the S_1 excited-state surface, suggesting that the character of the LR-TD-B3LYP PES is very different in the region above the S_0 minimum compared to the PES in the region of the S_1 minimum. This result is consistent with the results of the previous section that found substantial change in the LR-TDDFT electron density difference at the S_1 minimum compared to at the S_0 minimum. The vibronic spectrum obtained within the vertical gradient approach is much more narrow due to the small vibronic

shoulder peak; this same peak is almost as large as the 0-0 transition for the adiabatic Hessian approach, showing that the S_1 minimum likely undergoes a significant change in geometry, given the more intense vibronic peak.

The vibronic spectrum obtained within the vertical gradient approach shows good agreement with the AIMD trajectory–based approach that employs second order truncation of the cumulant expansion. This latter method goes beyond the harmonic approximation to the shape of the PES by sampling nuclear configurations that may occur in anharmonic regions of the PES, which may be responsible for the increased broadening compared to the vertical gradient approach. The good agreement between methods is perhaps not surprising since both methods are sampling the S_1 PES region directly above the S_0 minimum. Interestingly, if the same LR-TDDFT S_1 normal modes and displacements that characterize the vibronic spectrum are used to compute the spectrum within the second or third order truncation to the cumulant expansion of the linear response function within the GBOM, large changes in the spectrum suggest significant change in curvature of the ground- and excited-state PES and/or a large Duschinsky rotation, leading to non-Gaussian fluctuations of the energy gap (see SI, Figures S2-S4). These large differences in curvature or a large rotation of normal modes may be due to the symmetry breaking going from the ground state S_0 minimum to the LR-TD-B3LYP S_1 minimum.

Perhaps the most striking result of this work is the comparison of the spectra computed with the Hessian and normal modes of the ΔSCF PIMOM S_1 minimum to that computed from the LR S_1 minimum. Here we again see a large difference between the intensity of the vibronic shoulder peak, with the spectrum obtained with the PIMOM S_1 minimum normal modes in good agreement with both the vertical gradient and the AIMD trajectory–based methods, suggesting that all three of these methods are consistent in their treatment of the character of the S_1 state.

In Fig. 2b the same spectra are compared for computation with the CAM-B3LYP functional. Here we see much better agreement with all methods. The adiabatic Hessian LR-TD-

CAM-B3LYP and AIMD–based spectra computed from the LR-TD-CAM-B3LYP excitation energies are nearly indistinguishable. The CAM-B3LYP functional predicts a larger gap between the S_1 and S_2 states, suggesting that there is much less mixing of these two excited states and, as seen from the excitation energies and oscillator strengths, the LR-TD-CAM-B3LYP S_1 state maintains similar character in the region of the vertical transition and at both the LR and PIMOM S_1 minima.

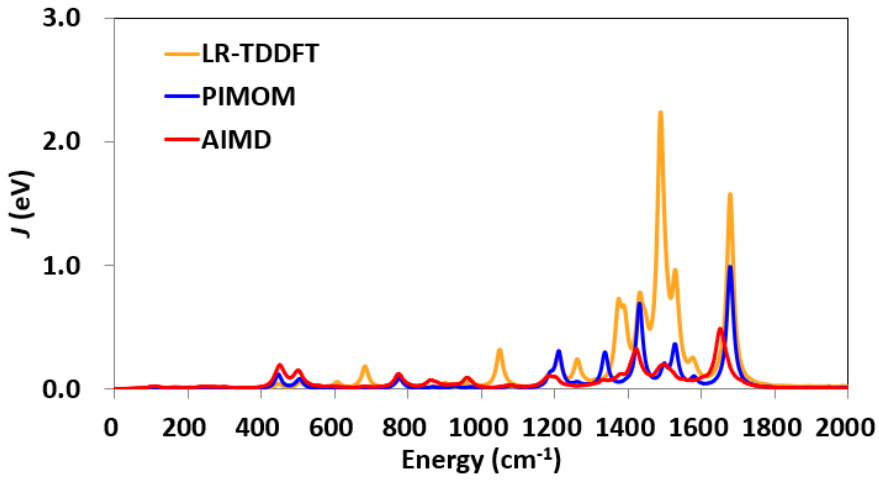

Figure 3: B3LYP S_0/S_1 spectral density computed using parameters from the LR-TDDFT and PIMOM normal modes from S_0 and S_1 optimized geometries, and that computed from the S_0 to S_1 energy gap time correlation function along the ground-state AIMD trajectory.

Plotting the spectral density allows us to compare how the different methods treat the modes that couple the S_0 and S_1 transition. The spectral densities in Fig. 3, computed from LR-TDDFT and PIMOM, are both obtained from a GBOM parametrized with the ground- and excited-state normal modes. We also show the spectral density computed from the energy gap time correlation function obtained from the AIMD trajectory. The spectral density based on the AIMD trajectory shows $\sim 10-20$ cm^{-1} red-shift of the peaks compared with the normal mode parametrization, due to the inclusion of anharmonicity of the PES in the vibrations of the chromophore. The spectral densities in Fig. 3 show that there is a high-intensity peak at around 1500 cm^{-1} in the LR-TDDFT spectral density, whereas the same region of the PIMOM and AIMD trajectory spectral density shows very little intensity.

This large peak of B_2 symmetry corresponds to the normal mode responsible for a significant amount of the large vibronic shoulder present in the adiabatic Hessian LR-TDDFT spectrum. This normal mode involves antisymmetric C-C stretches of the center ring coupled to the motion of the dimethyl amine groups. Because the LR-TD-B3LYP S_1 minimum is not of C_{2v} symmetry, contrary to other methods, this symmetry breaking leads to enhanced coupling with the anti-symmetric stretch, giving rise to the large peak in spectral density. We further analyze this normal mode in the following section.

4.3 Normal mode analysis

To analyze the nature of the S_1 and S_2 PESs along the B_2 anti-symmetric stretch normal mode motion, we performed a scan along this ground-state normal mode, computing both the LR-TDDFT and PIMOM energy gaps, shown in Fig. 4. The inset of Fig. 4(a) shows the normal mode vectors corresponding to the atomic displacements with an animation of the normal mode shown in the SI. The PES scan presents well-separated surfaces of the S_1 and S_2 states with PIMOM along the full normal mode displacement coordinate, unlike LR-TDDFT, where the surfaces are in close proximity at the minimum. Additionally, the shape of both the S_1 and S_2 LR-TDDFT PES along this mode clearly deviates from harmonic behavior, unlike the PIMOM PESs.

The LR-TDDFT oscillator strengths plotted in Fig. 4(b) show that at the S_0 minimum, S_1 is a bright state with oscillator strength $f \approx 0.8$, whereas the S_2 state is dark. As the atoms are displaced along this normal mode, the LR-TDDFT S_1 state loses oscillator strength and the LR-TDDFT S_2 state gains oscillator strength, showing that these two states mix together along this coordinate. At displacements of $\pm$ 0.2 au, the two states have nearly identical oscillator strengths of $f \approx 0.4$.

Overall, this normal mode analysis supports our finding above, that the character of the S_1 state is treated quite differently by adiabatic LR-TDDFT compared to PIMOM. The LR-TDDFT method leads to S_1 and S_2 state mixing in some regions of the PES, both along this

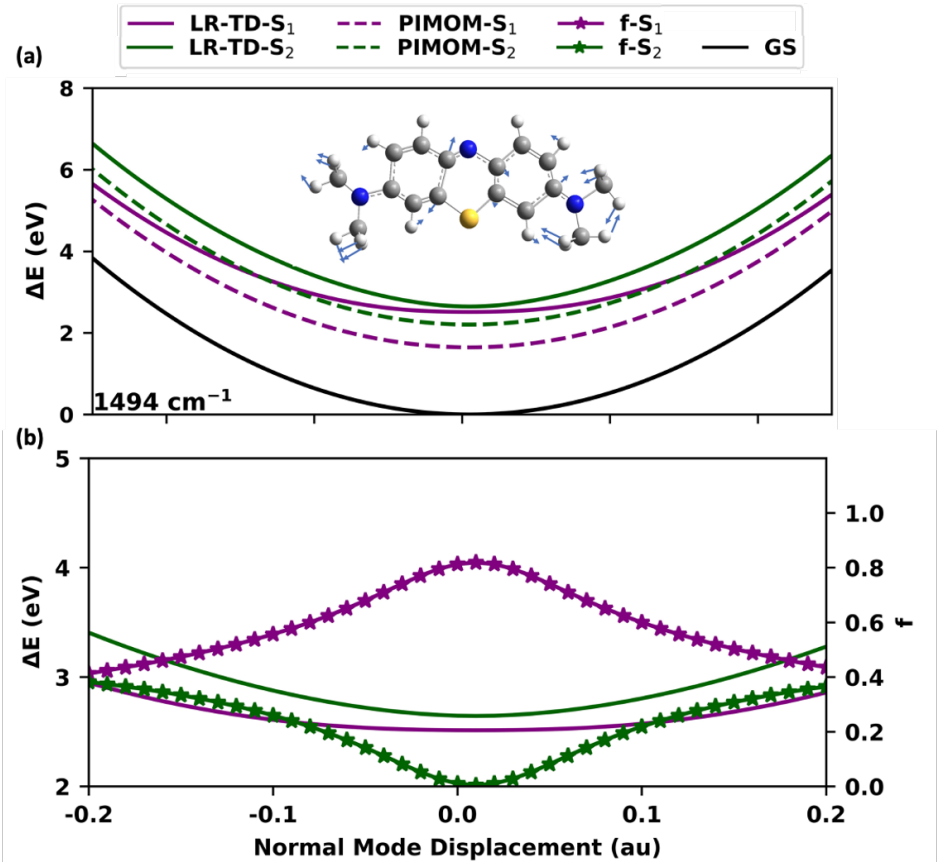

Figure 4: B3LYP potential surface scans of S_1 and S_2 states with respect to the ground state. (a) LR-TDDFT PESs are shown in solid lines, PIMOM PESs are shown in dashed lines, and ground state (GS) PES is drawn in black. The inset shows the displacement vectors for the ground state 1494 cm^{-1} B_2 asymmetric stretching mode. (b) For LR-TDDFT, the oscillator strengths are plotted with the energies along the normal mode displacement.

normal mode and at the S_1 minimum, whereas PIMOM maintains consistent S_1 character.

5 Conclusions

Calculating accurate optical spectra from first principles is essential for connecting spectroscopic experiments to the electronic characterization and dynamics of chromophores. The accuracy of the simulated spectra relies heavily on the quality of the excited-state calculation and the method chosen for computing the spectra. In this work, we compared the behavior of the widely used LR-TDDFT approach with PIMOM SCF results for computing the excited states of methylene blue, then applied a number of approaches for simulating the vibronic

spectra.

We find that the adiabatic LR-TD-B3LYP approach yields S_1 and S_2 states that mix together near the S_1 minimum. Although the S_1 state is bright and the S_2 state is dark at the ground state minimum, analysis of a key normal mode that strongly couples to the $S_0 \rightarrow S_1$ transition shows that the S_2 state borrows intensity from S_1 along this normal mode displacement, with S_1 and S_2 having nearly identical oscillator strengths at the S_1 minimum. In contrast, the PIMOM method produces diabatic states of consistent character across the PES, with a larger energy gap between S_1 and S_2. PIMOM also yields consistent character for both B3LYP and CAM-B3LYP S_1 PESs and electron densities, showing that it is less susceptible to density functional differences than the LR-TDDFT approach.

When applying these two excited state methods to the computation of vibronic spectra using a Hessian computed at the S_1 minimum, they yield very different results for methylene blue. The standard adiabatic Hessian LR-TD-B3LYP approach produces a very large vibronic shoulder in the spectrum, due to a change of character of the PES at the S_1 minimum because of the adiabatic treatment of the excited states. The spectra generated from LR-TD-B3LYP with a vertical gradient or an AIMD trajectory–based approach differ significantly from the adiabatic Hessian LR-TD3LYP approach, with no large vibronic shoulder. Large changes in the spectra with second and third order truncation of the cumulant expansion using the LR-TD-B3LYP S_1 parametrized GBOM suggest substantial changes in PES curvature or a large Duschinsky rotation matrix, with large mixing of normal mode coordinates possibly caused by the decrease in symmetry going from the S_0 C_{2v} to the LR-TD-B3LYP S_1 C_s minimum. In contrast, if the PIMOM method is used to compute S_1 minimum and corresponding Hessian and normal modes, the resulting vibronic spectrum is in excellent agreement with the vertical gradient and AIMD trajectory–based approaches, showing that all of these methods have a consistent treatment of the S_1 state in the region of the vertical excitation and at the PIMOM S_1 minimum. Switching from the B3LYP to the CAM-B3LYP functional increases the gap between the S_1 and S_2 states, with adiabatic Hes-

sian LR-TDDFT, PIMOM, and AIMD trajectory–based approaches all producing spectra in good agreement.

The large differences between the TD-B3LYP adiabatic Hessian and vertical gradient methods suggest the breakdown of the Born-Oppenheimer or harmonic approximation in the region of the LR-TD-B3LYP S_1 minimum. Indeed, the need for including non-adiabatic effects is supported by a recent study by some of the authors of solvated methylene blue that showed that there is significant population transfer from the S_1 state to the S_2 state upon photoexcitation, which is strongly coupled to the intensity of the vibronic shoulder.[46] Inclusion of this population transfer increases the vibronic shoulder, bringing the predicted spectrum more in line with experimental spectrum of aqueously solvated methylene blue.

Our results here point to the challenge of using an adiabatic excited-state approach for the computation of some excited-state properties, including the Hessian computed at an adiabatic excited-state minimum. Because adiabatic surfaces can change in character, the character of the state at the minimum may not accurately describe the system in the region of the vertical excitation. The state mixing seen here, and the resulting inconsistent description of the S_1 state, could be present with other adiabatic excited-state approaches. The use of a vertical gradient or AIMD energy gap time correlation function–based approach may more accurately describe the vertical excitation.

Overall, our study shows that the ΔSCF PIMOM approach produces states that are more aligned with a diabatic model, thus not subject to adiabatic state mixings that may lead to a change in PES character. In this study, the PIMOM Hessian method, vertical gradient LR method, and AIMD trajectory–based method all produced vibronic spectra in good agreement with each other. Given that PIMOM, in some cases, will be more computationally affordable than LR-TDDFT at finding an excited-state minimum, and depends less on the particular choice of functional, it offers an appealing alternative to the LR-TDDFT method for computing vibronic spectra.

Acknowledgement

The data that support the findings of this study are available from the corresponding authors upon request. This work was supported by the Department of Energy Basic Energy Sciences CTC and CPIMS programs (Grant No DE-SC0019053). Calculations were performed using the MERCED computational resource, supported by the National Science Foundation Major Research Instrumentation program (ACI-1429783). The spectral densities and cumulant spectra reported in this work were computed with the MolSpeckPy package available at https://github.com/tjz21/Spectroscopy_python_code.

Supporting Information Available

The Supporting Information includes CAM-B3LYP density differences, analysis of second and third order cumulant spectra, asymmetric stretch normal mode animation, tables of adiabatic and vertical excitation energies, optimized geometries.

References

(1) Ashford, D. L.; Gish, M. K.; Vannucci, A. K.; Brennaman, M. K.; Templeton, J. L.; Papanikolas, J. M.; Meyer, T. J. Molecular chromophore–catalyst assemblies for solar fuel applications. *Chem. Rev.* **2015**, *115*, 13006–13049.

(2) Sarkar, K.; Dhara, K.; Nandi, M.; Roy, P.; Bhaumik, A.; Banerjee, P. Selective zinc (II)-ion fluorescence sensing by a functionalized mesoporous material covalently grafted with a fluorescent chromophore and consequent biological applications. *Adv. Funct. Mater.* **2009**, *19*, 223–234.

(3) Fujimoto, K. J. Electronic Couplings and Electrostatic Interactions Behind the Light Absorption of Retinal Proteins. *Front. Mol. Biosci.* **2021**, 898.

(4) Linsley, C. S.; Quach, V. Y.; Agrawal, G.; Hartnett, E.; Wu, B. M. Visible light and near-infrared-responsive chromophores for drug delivery-on-demand applications. *Drug Deliv. Transl. Res.* **2015**, *5*, 611–624.

(5) Kanis, D. R.; Ratner, M. A.; Marks, T. J. Design and construction of molecular assemblies with large second-order optical nonlinearities. Quantum chemical aspects. *Chem. Rev.* **1994**, *94*, 195–242.

(6) Robinson, B. H.; Johnson, L. E.; Elder, D. L.; Kocherzhenko, A. A.; Isborn, C. M.; Haffner, C.; Heni, W.; Hoessbacher, C.; Fedoryshyn, Y.; Salamin, Y.; Baeuerle, B.; Josten, A.; Ayata, M.; Koch, U.; Leuthold, J.; Dalton, L. R. Optimization of Plasmonic-Organic Hybrid Electro-Optics. *J. Light. Technol.* **2018**, *36*, 5036–5047.

(7) Casida, M. E. Time-Dependent Density Functional Response Theory for Molecules. In *Recent Advances in Density Functional Methods*; World Scientific, 1995; pp 155–192.

(8) Bauernschmitt, R.; Ahlrichs, R. Treatment of electronic excitations within the adiabatic approximation of time dependent density functional theory. *Chem. Phys. Lett.* **1996**, *256*, 454–464.

(9) Furche, F.; Ahlrichs, R. Adiabatic time-dependent density functional methods for excited state properties. *J. Chem. Phys.* **2002**, *117*, 7433–7447.

(10) Parker, S. M.; Furche, F. Response Theory and Molecular Properties. In *Frontiers of Quantum Chemistry*; Springer Singapore: Singapore, 2018; pp 69–86.

(11) Laurent, A. D.; Jacquemin, D. TD-DFT benchmarks: A review. *Int. J. Quantum Chem.* **2013**, *113*, 2019–2039.

(12) Maitra, N. T.; Zhang, F.; Cave, R. J.; Burke, K. Double excitations within time-dependent density functional theory linear response. *J. Chem. Phys.* **2004**, *120*, 5932–5937.

(13) Cave, R. J.; Zhang, F.; Maitra, N. T.; Burke, K. A dressed TDDFT treatment of the 21Ag states of butadiene and hexatriene. *Chem. Phys. Lett.* **2004**, *389*, 39–42.

(14) Levine, B. G.; Ko, C.; Quenneville, J.; Martinez, T. J. Conical intersections and double excitations in time-dependent density functional theory. *Mol. Phys.* **2006**, *104*, 1039–1051.

(15) Elliott, P.; Goldson, S.; Canahui, C.; Maitra, N. T. Perspectives on double-excitations in TDDFT. *Chem. Phys.* **2011**, *391*, 110–119, Open problems and new solutions in time dependent density functional theory.

(16) Barca, G. M.; Gilbert, A. T.; Gill, P. M. Simple models for difficult electronic excitations. *J. Chem. Theory Comput.* **2018**, *14*, 1501–1509.

(17) Gilbert, A. T.; Besley, N. A.; Gill, P. M. Self-consistent field calculations of excited states using the maximum overlap method (MOM). *J. Phys. Chem. A* **2008**, *112*, 13164–13171.

(18) Zhan, C.-G. Maximum overlap method and the bond strength. *Int. J. Quantum Chem.* **1987**, *32*, 1–11.

(19) Maksić, Z.; Eckert-Maksić, M.; Randić, M. Correlation between CH and CC spin-spin coupling constants and s character of hybrids calculated by the maximum overlap method. *Theor. Chim. Acta* **1971**, *22*, 70–79.

(20) Cioslowski, J.; Challacombe, M. Maximum similarity orbitals for analysis of the electronic excited states. *Int. J. Quantum Chem.* **1991**, *40*, 81–93.

(21) Hait, D.; Head-Gordon, M. Excited state orbital optimization via minimizing the square of the gradient: General approach and application to singly and doubly excited states via density functional theory. *J. Chem. Theory Comput.* **2020**, *16*, 1699–1710.

(22) Carter-Fenk, K.; Herbert, J. M. State-Targeted Energy Projection: A Simple and Robust Approach to Orbital Relaxation of Non-Aufbau Self-Consistent Field Solutions. *J. Chem. Theory Comput.* **2020**, *16*, 5067–5082.

(23) Barca, G. M.; Gilbert, A. T.; Gill, P. M. Simple Models for Difficult Electronic Excitations. *J. Chem. Theory Comput.* **2018**, *14*, 1501–1509.

(24) Ramos, P.; Pavanello, M. Nonadiabatic couplings from a variational excited state method based on constrained DFT. *J. Chem. Phys.* **2021**, *154*, 014110.

(25) Corzo, H. H.; Abou Taka, A.; Aurora, P.-J.; Hratchian, H. P. Manuscript submitted for publication.

(26) Abou Taka, A.; Corzo, H. H.; Aurora, P.-J.; Hratchian, H. P. Unpublished Manuscript.

(27) Biczysko, M.; Bloino, J.; Santoro, F.; Barone, V. Time-Independent Approaches to Simulate Electronic Spectra Lineshapes: From Small Molecules to Macrosystems. In *Computational Strategies for Spectroscopy*; John Wiley & Sons, Ltd, 2011; Chapter 8, pp 361–443.

(28) Duschinsky, F. . *Acta Physicochim. URSS.* **1937**, *7*, 411.

(29) Santoro, F.; Lami, A.; Improta, R.; Bloino, J.; Barone, V. Effective method for the computation of optical spectra of large molecules at finite temperature including the Duschinsky and Herzberg–Teller effect: The Qx band of porphyrin as a case study. *J. Chem. Phys.* **2008**, *128*, 224311.

(30) Macak, P.; Luo, Y.; Ågren, H. Simulations of vibronic profiles in two-photon absorption. *Chem. Phys. Lett.* **2000**, *330*, 447–456.

(31) Mukazhanova, A.; Trerayapiwat, K. J.; Mazaheripour, A.; Wardrip, A. G.; Frey, N. C.; Nguyen, H.; Gorodetsky, A. A.; Sharifzadeh, S. Accurate first-principles calcula-

tion of the vibronic spectrum of stacked perylene tetracarboxylic acid diimides. *J. Phys. Chem. A* **2020**, *124*, 3055–3063.

(32) Hazra, A.; Chang, H. H.; Nooijen, M. First principles simulation of the UV absorption spectrum of ethylene using the vertical Franck-Condon approach. *J. Chem. Phys.* **2004**, *121*, 2125–2136.

(33) Hazra, A.; Nooijen, M. Vibronic coupling in the excited cationic states of ethylene: Simulation of the photoelectron spectrum between 12 and 18eV. *J. Chem. Phys.* **2005**, *122*, 204327.

(34) Avila Ferrer, F. J.; Santoro, F. Comparison of vertical and adiabatic harmonic approaches for the calculation of the vibrational structure of electronic spectra. *Phys. Chem. Chem. Phys.* **2012**, *14*, 13549–13563.

(35) Mukamel, S. *Principles of Nonlinear Optical Spectroscopy*; Oxford University Press: New York, 1995.

(36) Zuehlsdorff, T. J.; Montoya-Castillo, A.; Napoli, J. A.; Markland, T. E.; Isborn, C. M. Optical spectra in the condensed phase: Capturing anharmonic and vibronic features using dynamic and static approaches. *J. Chem. Phys.* **2019**, *151*, 074111.

(37) Zuehlsdorff, T. J.; Shedge, S. V.; Lu, S.-Y.; Hong, H.; Aguirre, V. P.; Shi, L.; Isborn, C. M. Vibronic and Environmental Effects in Simulations of Optical Spectroscopy. *Ann. Rev. Phys. Chem.* **2021**, *72*, 165–188, PMID: 33395546.

(38) Bader, J. S.; Berne, B. J. Quantum and classical relaxation rates from classical simulations. *J. Chem. Phys.* **1994**, *100*, 8359.

(39) Egorov, S. A.; Everitt, K. F.; Skinner, J. L. Quantum Dynamics and Vibrational Relaxation. *J. Phys. Chem. A* **1999**, *103*, 9494–9499.

(40) Kim, H.; Rossky, P. J. Evaluation of Quantum Correlation Functions from Classical Data. *J. Phys. Chem. B* **2002**, *106*, 8240.

(41) Valleau, S.; Eisfeld, A.; Aspuru-Guzik, A. On the alternatives for bath correlators and spectral densities from mixed quantum-classical simulations. *J. Chem. Phys.* **2012**, *137*, 224103.

(42) Zuehlsdorff, T.; Hong, H.; Shi, L.; Isborn, C. Nonlinear Spectroscopy in the Condensed Phase: The Role of Duschinsky Rotations and Third Order Cumulant Contributions. *J. Chem. Phys.* **2020**, *153*, 044127–16.

(43) Zuehlsdorff, T. J.; Hong, H.; Shi, L.; Isborn, C. M. Influence of Electronic Polarization on the Spectral Density. *J. Phys. Chem. B* **2020**, *124*, 531–543.

(44) Lu, S.-Y.; Zuehlsdorff, T. J.; Hong, H.; Aguirre, V. P.; Isborn, C. M.; Shi, L. The Influence of Electronic Polarization on Nonlinear Optical Spectroscopy. *J. Phys. Chem. B* **2021**, *0*, null.

(45) de Queiroz, T. B.; de Figueroa, E. R.; Coutinho-Neto, M. D.; Maciel, C. D.; Tapavicza, E.; Hashemi, Z.; Leppert, L. First principles theoretical spectroscopy of methylene blue: Between limitations of time-dependent density functional theory approximations and its realistic description in the solvent. *J. Chem. Phys.* **2021**, *154*, 044106.

(46) Dunnett, A. J.; Gowland, D.; Isborn, C. M.; Chin, A. W.; Zuehlsdorff, T. J. Influence of non-adiabatic effects on linear absorption spectra in the condensed phase: Methylene blue. *J. Chem. Phys.* **2021**, *155*, 144112.

(47) McWeeny, R. SCF theory for excited states: I. Optimal orbitals for the states of a configuration. *Mol. Phys.* **1974**, *28*, 1273–1282.

(48) Davidson, E. R.; Stenkamp, L. Z. SCF methods for excited states. *Int. J. Quantum Chem.* **1976**, *10*, 21–31.

(49) De Mello, P. C.; Hehenberger, M.; Zernert, M. Converging SCF calculations on excited states. *Int. J. Quantum Chem.* **1982**, *21*, 251–258.

(50) McCourt, M.; McIver Jr, J. W. On the SCF calculation of excited states: Singlet states in the two-electron problem. *J. Comput. Chem.* **1987**, *8*, 454–458.

(51) Barca, G. M.; Gilbert, A. T.; Gill, P. M. Communication: Hartree-Fock description of excited states of H_2. 2014.

(52) Ye, H.-Z.; Welborn, M.; Ricke, N. D.; Van Voorhis, T. σ-SCF: A direct energy-targeting method to mean-field excited states. *J. Chem. Phys.* **2017**, *147*, 214104.

(53) Doktorov, E. V.; Malkin, I. A.; Man'ko, V. I. Dynamical symmetry of vibronic transitions in polyatomic molecules and the Franck-Condon principle. *J. Mol. Spectrosc.* **1975**, *56*, 1–20.

(54) Berger, R.; Fischer, C.; Klessinger, M. Calculation of the vibronic fine structure in electronic spectra at higher temperatures. 1. Benzene and pyrazine. *J. Phys. Chem. A* **1998**, *102*, 7157–7167.

(55) Santoro, F.; Lami, A.; Improta, R.; Bloino, J.; Barone, V. Effective method for the computation of optical spectra of large molecules at finite temperature including the Duschinsky and Herzberg-Teller effect: The Qx band of porphyrin as a case study. *J. Chem. Phys.* **2008**, *128*, 224311.

(56) Baiardi, A.; Bloino, J.; Barone, V. General Time Dependent Approach to Vibronic Spectroscopy Including Franck–Condon, Herzberg–Teller, and Duschinky Effects. *J. Chem. Theory Comput.* **2013**, *9*, 4097–4115.

(57) de Souza, B.; Neese, F.; Izsák, R. On the theoretical prediction of fluorescence rates from first principles using the path integral approach. *J. Chem. Phys.* **2018**, *148*, 034104.

(58) Cerezo, J.; Avila Ferrer, F. J.; Prampolini, G.; Santoro, F. Modeling Solvent Broadening on the Vibronic Spectra of a Series of Coumarin Dyes. From Implicit to Explicit Solvent Models. *J. Chem. Theory Comput.* **2015**, *11*, 5810–5825.

(59) Anda, A.; De Vico, L.; Hansen, T.; Abramavičius, Absorption and Fluorescence Lineshape Theory for Polynomial Potentials. *J. Chem. Theory Comput.* **2016**, *12*, 5979–5989.

(60) Frisch, M. J.; Pople, J. A.; Binkley, J. S. Self-consistent molecular orbital methods 25. Supplementary functions for Gaussian basis sets. *J. Chem. Phys.* **1984**, *80*, 3265–3269.

(61) Seeger, R.; Pople, J. A. Self-consistent molecular orbital methods. XVIII. Constraints and stability in Hartree–Fock theory. *J. Chem. Phys.* **1977**, *66*, 3045–3050.

(62) Bauernschmitt, R.; Ahlrichs, R. Stability analysis for solutions of the closed shell Kohn–Sham equation. *J. Chem. Phys.* **1996**, *104*, 9047–9052.

(63) Casida, M. E.; Jamorski, C.; Casida, K. C.; Salahub, D. R. Molecular excitation energies to high-lying bound states from time-dependent density-functional response theory: Characterization and correction of the time-dependent local density approximation ionization threshold. *J. Chem. Phys.* **1998**, *108*, 4439–4449.

(64) Stratmann, R. E.; Scuseria, G. E.; Frisch, M. J. An efficient implementation of time-dependent density-functional theory for the calculation of excitation energies of large molecules. *J. Chem. Phys.* **1998**, *109*, 8218–8224.

(65) Frisch, M. J.; Trucks, G. W.; Schlegel, H. B.; Scuseria, G. E.; Robb, M. A.; Cheeseman, J. R.; Scalmani, G.; Barone, V.; Petersson, G. A.; Nakatsuji, H.; Li, X.;

Caricato, M.; Marenich, A. V.; Bloino, J.; Janesko, B. G.; Gomperts, R.; Mennucci, B.; Hratchian, H. P.; Ortiz, J. V.; Izmaylov, A. F.; Sonnenberg, J. L.; Williams-Young, D.; Ding, F.; Lipparini, F.; Egidi, F.; Goings, J.; Peng, B.; Petrone, A.; Henderson, T.; Ranasinghe, D.; Zakrzewski, V. G.; Gao, J.; Rega, N.; Zheng, G.; Liang, W.; Hada, M.; Ehara, M.; Toyota, K.; Fukuda, R.; Hasegawa, J.; Ishida, M.; Nakajima, T.; Honda, Y.; Kitao, O.; Nakai, H.; Vreven, T.; Throssell, K.; Montgomery, J. A., Jr.; Peralta, J. E.; Ogliaro, F.; Bearpark, M. J.; Heyd, J. J.; Brothers, E. N.; Kudin, K. N.; Staroverov, V. N.; Keith, T. A.; Kobayashi, R.; Normand, J.; Raghavachari, K.; Rendell, A. P.; Burant, J. C.; Iyengar, S. S.; Tomasi, J.; Cossi, M.; Millam, J. M.; Klene, M.; Adamo, C.; Cammi, R.; Ochterski, J. W.; Martin, R. L.; Morokuma, K.; Farkas, O.; Foresman, J. B.; Fox, D. J. Gaussian Development Version, Revision J.05. 2020; Gaussian Inc. Wallingford CT.

(66) Thompson, L. M.; Harb, H.; Hratchian, H. P. Natural ionization orbitals for interpreting electron detachment processes. *J. Chem. Phys.* **2016**, *144*, 204117.

(67) Harb, H.; Hratchian, H. P. ΔSCF Dyson orbitals and pole strengths from natural ionization orbitals. *J. Chem. Phys.* **2021**, *154*, 084104.

(68) Harb, H.; Hratchian, H. P. Natural ionization orbitals. 2020; `https://github.com/HratchianGroup/niorep`.

(69) Martin, R. L. Natural transition orbitals. *J. Chem. Phys.* **2003**, *118*, 4775–4777.

(70) Sonnenberg, J. L.; Schlegel, H. B.; Hratchian, H. P. Spin Contamination in Inorganic Chemistry Calculations. In *Encyclopedia of Inorganic and Bioinorganic Chemistry*; American Cancer Society, 2011; pp 173–186.

(71) Saito, T.; Nishihara, S.; Kataoka, Y.; Nakanishi, Y.; Matsui, T.; Kitagawa, Y.; Kawakami, T.; Okumura, M.; Yamaguchi, K. Transition state optimization based on approximate spin-projection (AP) method. *Chem. Phys. Lett.* **2009**, *483*, 168–171.

(72) Saito, T.; Ito, A.; Watanabe, T.; Kawakami, T.; Okumura, M.; Yamaguchi, K. Performance of the coupled cluster and DFT methods for through-space magnetic interactions of nitroxide dimer. *Chem. Phys. Lett.* **2012**, *542*, 19–25.

(73) Ferré, N.; Guihéry, N.; Malrieu, J.-P. Spin decontamination of broken-symmetry density functional theory calculations: deeper insight and new formulations. *Phys. Chem. Chem. Phys.* **2015**, *17*, 14375–14382.

(74) Thompson, L. M.; Hratchian, H. P. Modeling the Photoelectron Spectra of $MoNbO_2^-$-Accounting for Spin Contamination in Density Functional Theory. *J. Phys. Chem. A* **2015**, *119*, 8744–8751.

(75) Sheng, X.; Thompson, L. M.; Hratchian, H. P. Assessing the Calculation of Exchange Coupling Constants and Spin Crossover Gaps Using the Approximate Projection Model to Improve Density Functional Calculations. *J. Chem. Theory Comput.* **2019**, *16*, 154–163.

(76) Thompson, L. M.; Hratchian, H. P. Spin projection with double hybrid density functional theory. *J. Chem. Phys.* **2014**, *141*, 034108.

(77) Thompson, L. M.; Hratchian, H. P. Second derivatives for approximate spin projection methods. *J. Chem. Phys.* **2015**, *142*, 054106.

(78) Hratchian, H. P. Communication: An efficient analytic gradient theory for approximate spin projection methods. *J. Chem. Phys.* **2013**, *138*, 101101.

(79) Hratchian, H.; Schlegel, H. Theory and Applications of Computational Chemistry: The First 40 Years. *Dykstra, CE* **2005**, 195–249.

(80) Schaefer III, H. F.; Yamaguchi, Y. A new dimension to quantum chemistry: Theoretical methods for the analytic evaluation of first, second, and third deriva-

tives of the molecular electronic energy with respect to nuclear coordinates. *J. Mol. Struct.: THEOCHEM* **1986**, *135*, 369–390.

(81) Stratmann, R. E.; Burant, J. C.; Scuseria, G. E.; Frisch, M. J. Improving harmonic vibrational frequencies calculations in density functional theory. *J. Chem. Phys.* **1997**, *106*, 10175–10183.

(82) Santoro, F.; Improta, R.; Lami, A.; Bloino, J.; Barone, V. Effective method to compute Franck-Condon integrals for optical spectra of large molecules in solution. *J. Chem. Phys.* **2007**, *126*, 084509.

(83) Zuehlsdorff, T. J. MolSpeckPy: Spectroscopy python code, available on Github: https://github.com/tjz21/Spectroscopy_python_code. 2021; `https://github.com/tjz21/Spectroscopy_python_code`.

(84) Medders, G. R.; Alguire, E. C.; Jain, A.; Subotnik, J. E. Ultrafast Electronic Relaxation through a Conical Intersection: Nonadiabatic Dynamics Disentangled through an Oscillator Strength-Based Diabatization Framework. *J. Phys. Chem. A* **2017**, *121*, 1425–1434.